

# Measurement of ion temperature and toroidal flow during magnetic reconnection with a large guide field

Cite as: Phys. Plasmas **30**, 112104 (2023); doi: [10.1063/5.0140781](https://doi.org/10.1063/5.0140781)  
Submitted: 30 December 2022 · Accepted: 20 September 2023 ·  
Published Online: 10 November 2023








View Online



Export Citation



CrossMark

A. Goodman,<sup>1,a)</sup>  H. Ji,<sup>2,3</sup>  S. Bose,<sup>3</sup>  J. Yoo,<sup>3</sup>  and A. Alt<sup>3</sup> 

## AFFILIATIONS

<sup>1</sup>Department of Mechanical and Aerospace Engineering, Princeton University Mechanical and Aerospace, Engineering Room D-209 A/B—Business Center—Engineering Quad Olden Street Princeton, New Jersey 08544-5263, USA

<sup>2</sup>Department of Astrophysical Sciences, Princeton University, 4 Ivy Ln, Princeton, New Jersey 08544-5263, USA

<sup>3</sup>Princeton Plasma Physics Laboratory, Princeton University, 100 Stellarator Road, Princeton, New Jersey 08540, USA

<sup>a)</sup>Author to whom correspondence should be addressed: [aagoodma@pppl.gov](mailto:aagoodma@pppl.gov)

## ABSTRACT

Ion temperature and toroidal flow along the guide field direction are measured using a new ion tomographic diagnostic on the Magnetic Reconnection eXperiment (MRX) during magnetic reconnection with a guide field strength of about 1.4 and 2.1 times the strength of the reconnecting component. Strong toroidal flows, beyond what has been measured in anti-parallel and lower guide field conditions on MRX, are observed. Sustained ion heating with no discernible structure within the measurement region is also observed. Probe measurements including Langmuir and Mach probe measurements are made to support the tomographic inversion of line-integrated measurements, as well as to provide local measurements of plasma parameters. Measurements of toroidal velocity and ion temperature are supported with time series data. Energy flow into and out of the X-line region is estimated using a guiding center framework and presented in the Appendix of this manuscript, suggesting an outsized role played by parallel electric field in energizing ions. The guiding center approximation is not well satisfied in the region of interest; however, the estimates provide a springboard for future, further experimentation.

Published under an exclusive license by AIP Publishing. <https://doi.org/10.1063/5.0140781>

## I. INTRODUCTION

Magnetic reconnection is a fundamental plasma process in which stored magnetic energy is converted to plasma kinetic energy, while magnetic field topology is changed. Most instances of magnetic reconnection observed in nature occur in the presence of a finite component of the magnetic field perpendicular to the reconnection plane.<sup>1</sup> This component of the magnetic field is known as a guide field (GF),  $B_{GF}$ , and is thought to have an impact on energization of electrons and ions. Kinetic theory and numerical simulations suggest that a large guide field<sup>2</sup> may impact the efficiency of ion heating and acceleration, and prominent ion heating has been observed during merging experiments in the presence of a strong guide field.<sup>3</sup> The high GF conditions reported in this article are similar to those observed during reconnection in earth's magnetosphere,<sup>4–6</sup> solar wind,<sup>7</sup> and solar flares<sup>8</sup> as well as a variety of reconnection and fusion-related laboratory experiments.<sup>9–11</sup>

Ion temperature and flow are of paramount importance in understanding energy conversion to ions during magnetic reconnection.<sup>12</sup> The recent development of a new tomographic Ion Doppler

spectroscopy system<sup>13</sup> for the Magnetic Reconnection eXperiment (MRX)<sup>14</sup> has enabled, for the first time on MRX, the simultaneous measurement of ion temperature and out-of-plane flow over an extended distance across the reconnecting current sheet. Compared to the Ion Doppler Spectroscopy Probe (IDSP),<sup>15</sup> previously used for a single-point measurements on MRX, this diagnostic has improved resolution and is more efficient in collecting ion temperature and velocity profiles. Previous work from the University of Tokyo has demonstrated the viability of line-integrated measurements for these purposes and has measured ion heating both inside and out of the current sheet.<sup>10</sup>

Previous work in anti-parallel regimes suggests that roughly two-thirds of converted magnetic energy is transferred to ions during the reconnection process.<sup>16</sup> Recent work from Bose *et al.*<sup>9</sup> addresses energization in the weak guide field regime ( $B_{GF}$  is about 0.7 times of the reconnecting component,  $B_{rec}$ ). However, until now no systematic study of energy conversion has been done in a high-GF regime. Previous numerical studies of high guide field reconnection have

suggested possible mechanisms including pickup-like mechanisms,<sup>17</sup> stochastic heating,<sup>18</sup> and direct acceleration by the parallel electric field along the magnetic field,  $E_{\parallel}$ .<sup>19,20</sup> Additionally, measurements of localized, kinetic scale physics from a small number of spacecraft suggests ions may be heated during GF reconnection, with no conclusive mechanism yet identified.<sup>4-6,21</sup>

In this article, profiles of ion temperature and out of plane ion flow are presented for high guide field magnetic reconnection in MRX,  $B_{GF} \approx 1.4B_{rec}$  or  $2.1B_{rec}$ . Possible ion energization mechanisms are discussed including quantitative estimation of the effectiveness of each proposed mechanism in MRX. Estimates of some mechanisms are based in guiding center theory which is only weakly satisfied in the region of interest. For this reason, estimates should be viewed not as conclusions, but rather as important information for further experimentation. It is estimated that of all the mechanisms examined, the parallel electric field,  $E_{\parallel}$  has the greatest impact on ion energization. The rest of this paper is structured as follows: the experimental setup and an overview of *in situ* probes are outlined in Sec. II; the setup, alignment, and algorithm behind the updated Ion Doppler tomography diagnostic from Goodman *et al.*<sup>13</sup> are discussed in Sec. III. Plasma conditions and measurement results for each GF condition are presented in Sec. IV. An estimation of various energization mechanisms is made in Appendix, and finally, a discussion of measurements shown and estimates made in Appendix is provided in Sec. V.

## II. EXPERIMENTAL SETUP

MRX is a cylindrical vacuum vessel with a radius of 76.2 cm and five sets of coils that produce plasma and the magnetic configuration necessary for reconnection studies. The MRX coordinate system and geometry is shown in Fig. 1. The  $z$  coordinate runs along the axial direction of the device, the  $\phi$  coordinate runs in the direction

perpendicular to the reconnection plane, and the  $r$  coordinate completes the right-handed coordinated system. Throughout the paper, velocity in the out-of-plane,  $\phi$  direction is labeled as  $v_{\phi}$  or toroidal velocity as is convention on MRX. During operation, toroidal field (TF) coils, housed in the flux cores, produce an inductive electric field that causes plasma breakdown. The poloidal field (PF) coils, also housed in flux cores, create the magnetic geometry necessary to study reconnection. An axially-directed set of coils, running through the bottom of Fig. 1, is responsible for generating the guide field (GF) in the  $\phi$  direction. Equilibrium field (EF) coils denoted in Fig. 1 control the location of the current sheet in the  $r$  direction for reproducible measurements. Finally, toroidal coils running around the GF coils (drive coils) provide extra drive for reconnection, which can be substantially reduced without these coils during high GF experiments. In this experiment, the TF coils are arranged in a “counter-helicity” configuration that minimizes contributions to the GF from sources other than the GF coils.<sup>14,22</sup>

For this experiment, Helium is utilized as a working gas. A variety of *in situ* probes are used throughout the experiment to measure the magnetic field, the out-of-plane electric field component, electron density and temperature, floating potential, and radial and axial velocity of ions. Eight magnetic “B-dot” probes measure all three components of the magnetic field at  $0.4 \mu s$  time intervals with coverage from  $z = -9$  cm to  $z = 9$  cm.<sup>23</sup> Figure 2 shows a standard flux plot (contours) overlaid on a color plot of the GF for both conditions studied for this experiment. The asymmetry of the guide field is not fully understood at this time; however, it is suggested that this structure is an artifact of the so-called “counter helicity operation,” due to the persistence of the field asymmetry at early periods of the discharge.

Two reference Langmuir probes, located at  $z = -1.5$  cm and  $r = 27.5$  and  $42.5$  cm, are used to monitor shot-to-shot variation. One Langmuir probe was systematically scanned across the measurement region from  $z = -4.5$  cm to  $z = 6$  cm and from  $r = 30.5$  cm to  $r = 42.5$  cm. The same scans were performed with axial and radial Mach probes to measure the axial velocity,  $v_{iz}$ , and radial velocity,  $v_{ir}$ , respectively. Finally, a radial floating potential probe, capable of measuring floating potential at 17 radial locations for each shot, was scanned from  $z = -6$  cm to  $z = 9$  cm.<sup>16</sup> The summation of these probe measurements, including information about density, electron temperature,  $v_z$ ,  $v_r$ , and in-plane electric fields, is used in Sec. IV to help evaluate the importance of a variety of different energization mechanisms at each condition measured. For each  $(r, z)$  position on the probe measurement grid, at least 15 shots were taken at identical conditions to achieve appropriate statistics. The remaining diagnostic, integral to this experiment, is a new ion Doppler tomography diagnostic developed for MRX and the upcoming Facility for Laboratory Reconnection Experiments (FLARE).<sup>24</sup> This diagnostic is described in detail in Sec. III.

In this experiment, two GF strengths are explored:  $B_{GF} \approx 1.4B_{rec}$  and  $2.1B_{rec}$ , referred to as “GF 1.4” and “GF 2.1,” respectively. The nominal strength of the guide field is calculated as the ratio between the strength of the out-of-plane magnetic field at the null point and the reconnecting field in the upstream region, as defined in Figs. 2 and 9. Figure 2 shows typical contours of poloidal flux, obtained by properly integrating the measured magnetic field profiles for both conditions, which are stronger GF values that have been previously studied on MRX. Dataset selection restricts the data shown to shots in which the normalized GF remains within 15% of the nominal values.

10 November 2023 16:29:01

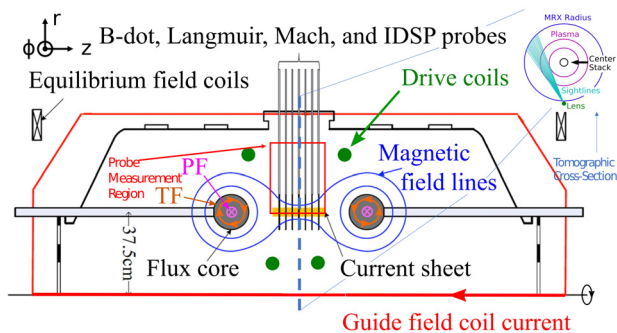


**FIG. 1.** Schematic showing coils responsible for MRX operation, right-handed coordinate system used during the experiment, and positions of *in situ* probes. The coordinate system is  $(r, z, \phi)$ , with the  $z$  coordinate running along the axial direction of the cylindrical vessel, in the same direction as the GF current. The  $\phi$  coordinate is defined perpendicular to the measured reconnection plane, and the  $r$  coordinate completes the right-handed coordinated system. The role of each coil set is detailed in the text below. Electrostatic probes are inserted through a port on the 3 o'clock position of the device and run along the  $r$  direction denoted in the figure, covering the measurement region described in red in the center of the figure. The Ion Doppler diagnostic (not shown in the figure) is placed at the 6 o'clock position of the device and lines of sight travel the  $r$ - $y$  plane at variable  $z$  locations from  $z = +5$  cm to  $z = -5$  cm. A schematic of the Ion Doppler diagnostic measurement cross section at a constant  $z$  location is shown as an inset in the top right of the figure.

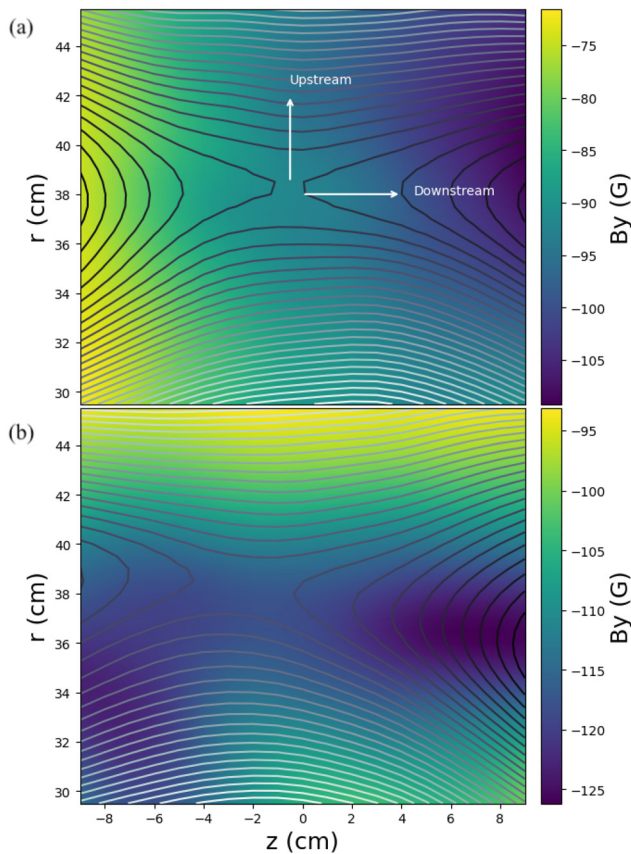


**FIG. 2.** Flux plots (contour) and GF strength (color plot) of two GF conditions measured in this experiment. (a): Magnetics for  $B_{GF} = 1.4B_{rec}$  (b): Magnetics for  $B_{GF} = 2.1B_{rec}$ . Arrows and labels in FIG (a) introduce the directions and concept of upstream and downstream regions used throughout this manuscript. The asymmetry in field strength for both conditions is thought to be an artifact of counter-helicity operation.

### III. DIAGNOSTIC SYSTEM

For this experiment and future experiments on MRX and FLARE, a tomographic ion Doppler diagnostic was constructed based on improvements from the proof of concept diagnostic described in Goodman *et al.*<sup>13</sup> This measurement system, built for an axisymmetric plasma configuration, is comprised of collection optics, a patch panel, fiber optic relays, a spectrometer, and a detector.

#### A. Hardware

The collection optics are comprised of 80, 400  $\mu\text{m}$  core diameter fibers with outer cladding diameters of 560  $\mu\text{m}$  and a numerical aperture of 0.39. The fibers are arranged linearly with 680  $\mu\text{m}$  center-to-center spacing, on the face of a cylindrical ferrule with a 2 cm radius. The ferrule sits at a depth of 46.5 mm behind a 50 mm focal length camera lens (NIKKOR Model#FBA\_2137) focused on the central tangency radius inside the vessel. This configuration enables measurements across an arc of  $36.8^\circ$  with a spatial resolution of  $\sim 0.75$  cm and a spot size, at the device midplane, of  $\sim 0.8$  cm. Spatial resolution

for this diagnostic describes the difference between tangency radius values of adjacent viewing chords.

Passing necessary photons to the detector in order to resolve low-temperature measurements in MRX required construction of a new spectrometer, utilizing an Andor Volume Phase Holographic (VPH) grating<sup>25</sup> with an F/# of 1.8. The optics of the spectrometer are designed around a 66 channel input. 66, 400  $\mu\text{m}$  core diameter fiber optic cables with outer cladding diameters of 560  $\mu\text{m}$  and a numerical aperture of 0.39 are arranged in three linear rows of 22 fibers each on the face of a cylindrical ferrule with a 1 cm radius. The height of the arrays is 11.76 mm and the arrays are spaced laterally on the ferrule face in such a way to maximize the separation between He-II lines in the detector image. In its current form, the spectrometer utilizes two Nikon 85 mm lenses with manual adjustments for focus and aperture and an F/# of 1.8. Matching lenses ensures 1:1 magnification. The detector utilized in this experiment is a PI-MAX2 Intensified Charged Coupled Device (ICCD) detector  $1024 \times 1024$  pixel<sup>2</sup> grid with 13.1  $\mu\text{m}$  pixel width and a quantum efficiency of 47%. A slit with a width of 45  $\mu\text{m}$  is placed in front of each array enabling resolution of ion temperatures of 5 eV or greater, and toroidal velocities of  $\geq 4$  km/s in  $\approx 0.75$  cm increments, with gate times of  $\leq 10$   $\mu\text{s}$  or less.

Spectrometer alignment and calibration is done using laser light, a neon calibration lamp, and a helium calibration lamp. Position and orientation of the input ferrule is controlled by a 3-axis translation stage and a precision rotation mount with 5 arc min fine-adjustment (ThorLabs PRM1). The detector position is controlled by a 3-axis translation stage and 3-axis tip/tilt/rotation stage with 2 arc min fine-adjustment (Newport Optics model37). The neon calibration lamp is used for final calculations of instrumental width and device dispersion. Results for a single row of pixels are shown panels (a) and (b) in Fig. 3. Panel (a) shows the raw image with annotations for the centerline of the detector (row 512) as well as the image center for a variety of measurable Neon lines across the detector. Panel (b) shows the measured pixel of wavelength centers and the associated dispersion calculation, while panel (c) shows the average instrumental width for each input channel with Channel 1 representing the top of the detector and Channel 22 representing the bottom of the detector. Beyond spectrometer calibration, the end-to-end transmission of the system was measured using an integrated light source (LabSphere URS600-H) illuminating the collection optics through the window on the bottom of the device. Normalizing the transmission of each channel by its respective connection into the spectrometer ensures consistency in inversion results.<sup>26</sup>

#### B. Tomographic inversion

The tomographic inversion algorithm used for this diagnostic involves a least squares minimization of collected data, run through an emission model to produce plasma profiles of emissivity, toroidal velocity, and ion temperature. In this model, an axisymmetric plasma is assumed with no emission outside of the measured area. It is assumed that lines of sight do not have a component in the  $z$ -direction of the machine. The presence of radial velocity in MRX, represented as the reconnection inflow, complicates traditional inversion techniques used in plasma physics such as wavelength-by-wavelength inversion.<sup>10</sup> Bell<sup>27</sup> has demonstrated a matrix-method for inverting tomographic measurements of axisymmetric plasmas in the presence of radial flows; however, the technique was not well suited to conditions present in MRX.



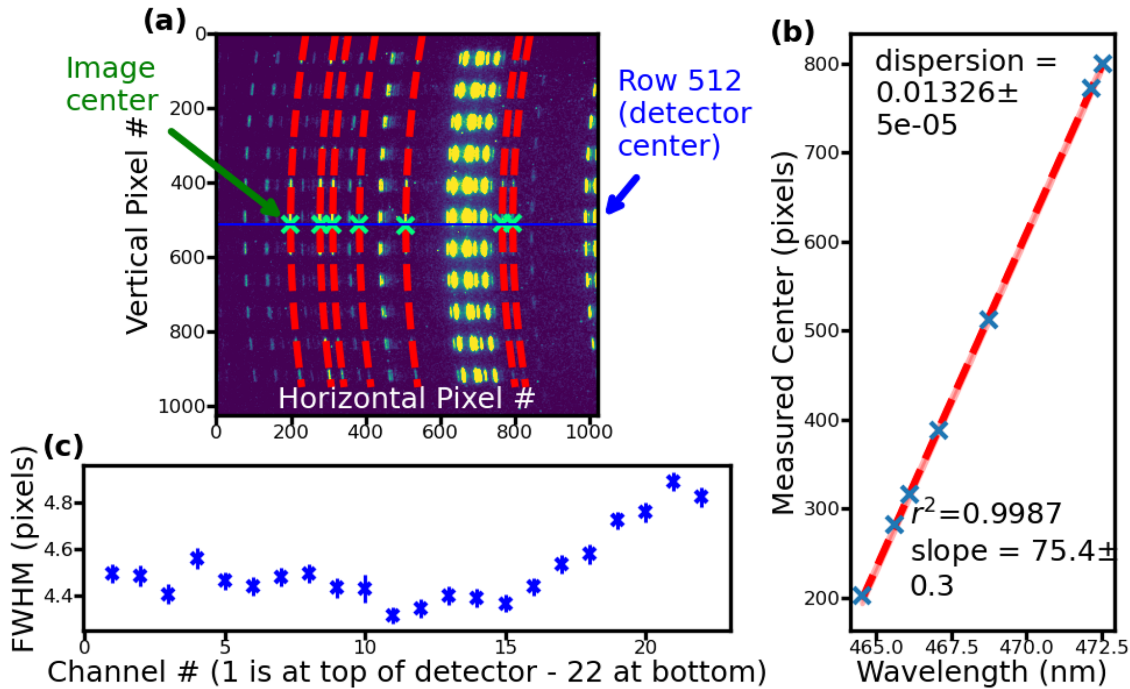


**FIG. 3.** Various images related to spectrometer alignment and calibration. Panel (a) shows a raw image from the Neon calibration lamp with a measured parabolic images of seven singlet lines used for calibration. Panel (b) shows the instrumental dispersion calculated for row 668 based on measured line centers for each of the seven lines, and panel (c) shows the average instrumental temperature for each channel, averaged over all rows of the channel for the three lines closes to  $\lambda = 468.570$  nm.

Bell’s algorithm is extended to a least squares minimization technique for the inversion of measurements made in this experiment. Algorithmic performance is tested under various conditions relevant to the plasma conditions of this experiment.

The inversion begins with measurements, calibrated by the above methods to remove differences in transmission between channels, instrumental broadening from the detector, and detector shift due to shot vibrations. These measurements are modeled as line integrated measurements,  $B_i$ , of spectral radiance,  $E(r, \lambda)$  from Bell.<sup>27</sup>

$$B_i(\lambda) = \oint E(r, \lambda) dl_i, \quad (1)$$

where  $\lambda$  is wavelength and the length element,  $dl_i$  refers to the path along sightline “i.” The spectral radiance is modeled for an axisymmetric plasma as

$$E(r, \lambda) = \frac{E_0(r)}{w(r)} \sqrt{\frac{4 \ln 2}{\pi}} \exp \left[ -4 \ln 2 \frac{\left( \lambda - \lambda_0 - \lambda_0 \left| \hat{s}_i \cdot \frac{v(r)}{c} \right| \right)^2}{w^2(r)} \right], \quad (2)$$

where  $c$  is the constant for speed of light;  $r$  is the radial coordinate;  $E_0$  is the scalar emissivity of the plasma;  $2w$  represents the full width at half max (FWHM) of the spectra, attributable to thermal broadening;  $\lambda_0$  is the rest wavelength of the line of interest, in the case 468.570 nm for He II;  $\hat{s}_i$  is the unit vector in the direction of the line of sight “i”; and  $v$  is the local flow. Doing traditional, matrix-style inversions on

moments of these spectra is an efficient and accurate method of inversion in hot plasmas with plenty of emission.<sup>27</sup> In MRX, however, the ion temperatures range from 5 to 15 eV, and subsequently, the emission is much dimmer than in fusion plasmas, for example. To increase the range of brightness invertible by this diagnostic, a different method was used.

The profiles of interest,  $E_0(r)$ ,  $v(r)$ , and  $w(r)$ , are first represented by Chebyshev polynomials of order 9. The degree of the polynomial is important for both computation time and accuracy of results. Higher order polynomials produce more exact results, at the cost of accuracy as they have the freedom to produce sharp gradients, not natural to measured plasma quantities in MRX. Polynomials of order 5 or less do not have the degrees of freedom necessary to reproduce results with spatial structure in MRX. With empirical and numerical testing, the optimal order for use on MRX was chosen as 9. The selection was made through detailed study of clean profiles at both GF conditions. Fifty smooth profiles from each condition were inverted using polynomial orders from 3 to 50. The results were averaged, and the normalized residual value vs polynomial order is shown in Fig. 4. Order 9 resides very close to the inflection point, where higher order polynomials begin to provide diminishing returns. Further, it was determined empirically that higher order polynomials showed increased prevalence of Runge’s phenomenon whereby oscillations in the inverted profile produce more exact results (lower residuals) at the expense of physically realistic lineshapes. The polynomial order should be reexamined for implementation on each specific application. To properly utilize this representation, the profiles are normalized and the radial domain is translated and scaled to the interval  $[-1, 1]$ .

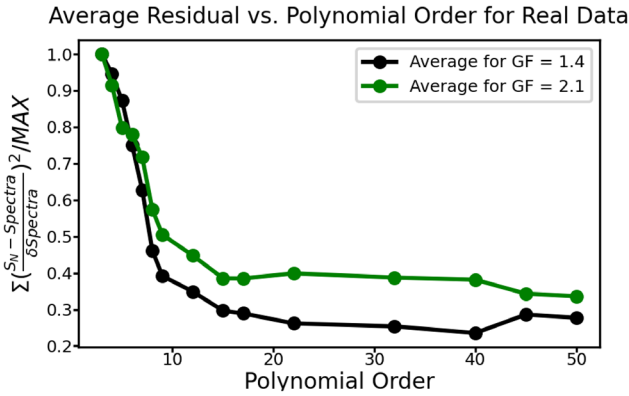


**FIG. 4.** A plot of normalized residual value vs polynomial order averaged over 50 shots for each GF condition. The plot clearly shows diminishing returns for higher order polynomials. Manual review of inversion results also showed increased prevalence of Runge’s phenomenon at higher order polynomials, which lowered the overall residual value at the expense of physically plausible profiles. Between the numerical evaluation of many shots, and the manual review of results, it was determined that order 9 polynomials offer the best marriage of accuracy and efficiency for the plasma conditions studied.

The inversion then proceeds by using a least squares technique using a trust region reflective algorithm minimization<sup>28</sup> to find the optimal coefficients for each profile simultaneously. This is achieved by using a residual function comparing measured spectra to synthetically created spectra using Eqs. (1) and (2).

Radial velocity is of particular importance as it is often incorrectly treated, or ignored all together, in other inversion processes for ion tomography in plasmas.<sup>13</sup> For this experiment, it is assumed that each sightline contains no component in the  $z$  direction, or equivalently

$$\hat{s}_i = s_r \hat{r} + s_\phi \hat{\phi} + 0\hat{z}, \quad (3)$$

which reduces the inner product,  $\hat{s}_i \cdot \mathbf{v}(r)$  to  $v_r(r) \cos \theta_r + v_\phi(r) \cos \theta_\phi$ , where  $\theta_r$  and  $\theta_\phi$  are the angles between the sightline and each velocity component. The two angles are related by a  $\pi/2$  phase shift. For real-time data analysis,  $v_r(r)$  is estimated by the radial component of  $\mathbf{E} \times \mathbf{B}$ . In post-processing, 2D radial velocity profiles measured from *in situ* probes are used as input for more exact inversions. Future improvements to this diagnostic should include another view, with another detector, which would permit for the inversion of two components of flow.

An important nuance in working with Helium plasmas is the consideration of Helium’s fine structure around the He-II 468.570 nm line. Properly removing the instrumental function from a measured spectra requires a fitting of the measured spectra. In this experiment, detailed fittings including multiple Gaussian functions, up to one per transition for each element of Helium’s fine structure, following a previous IDSP procedure demonstrated by Yoo,<sup>23</sup> were tested and results were compared to simpler single, double, and triple Gaussian fittings. It was determined from over 300 samples that the inclusion of each fine structure line produced results that were within 5% or less of the results from double Gaussian fittings, but took over 10 times as long to process. Thus, with thousands of shots to analyze, the decision was made to use double Gaussian fittings in the analysis of measured spectra.

The numerical algorithm is tested using Monte Carlo simulations with 10 000 trials under plasma conditions relevant to the given experiment. Multiple profiles of plasma emissivity, ion temperature, and two-component velocity are numerically constructed to simulate possible conditions in MRX. Wide parabolic and Gaussian profiles with both single and multiple peaks are used to represent  $T_i$  and  $v_\phi$ . A functional form of smoothed measurements of  $v_r = \mathbf{E} \times \mathbf{B}$  at the GF = 1.4 condition is used to represent  $v_r$ . Lines of sight relevant to this experimental condition are utilized in the  $r - \phi$  plane to construct numerical measurements that are inverted to recover scalar emissivity, ion temperature and toroidal velocity. The input into the inversion is the radial component of the flow. To test the algorithmic performance Fig. 5 shows the percentage error in both  $T_i$  as well as  $v_\phi$  inversions from the referenced algorithm vs maximum photon count in panel (a). Panel (b) shows the percentage error in the  $T_i$  inversion vs radial velocity strength (maroon) and uncertainty (dark cyan). To dark cyan, plot of panel (b) is obtained by introducing an error to the radial velocity profile used as an inversion input. The introduced error,  $\sigma_{v_r}$ , is defined as a percentage of the function value,  $v_r$ . The errors in Fig. 5 are calculated as

$$E_{total} = \sqrt{\frac{\sum_{i=1}^n (X_{target,i} - X_{inversion,i})^2}{X_{target,i} n - 1}}. \quad (4)$$

Although the edge of the plasma is poorly defined at the two guide field conditions investigated in this experiment, emission drops to undetectable levels beyond  $R = 45.5$  cm in most of the data

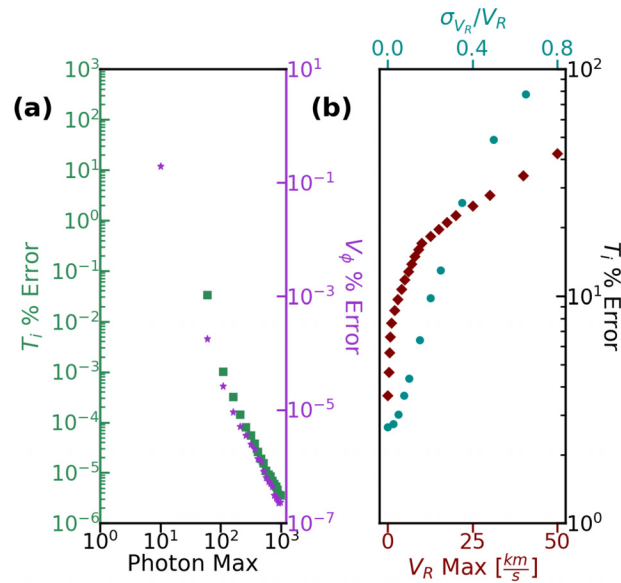


**FIG. 5.** Monte Carlo simulations ( $n = 10\,000$ ) of three different sources of error for the least squares inversion method used in this experiment. All plots show results for 22 measurement chords. Subplot (a) shows the total percentage error in  $T_i$  and  $V_\phi$  inversions vs the total photon count of the brightest measurement. A peak radial velocity magnitude of 15 km/s, and a peak  $T_i$  of 20 eV is used for subplot (a). Subplot (b) shows the total error vs magnitude of radial velocity,  $v_r$  in a 22 chord inversion of  $T_i$  with a peak photon count of 100 in maroon and show’s the total error of the  $T_i$  inversion vs the fractional standard deviation of  $v_r$  measurements for a 22-chord inversion in the dark cyan.

collected. No boundary condition is applied during the experiment, and the precise location of the plasma boundary is generally not important. In some instances, however, non-negligible emission beyond the outermost chord creates untenable errors in the experiment. Therefore, the relevant range of tangency radii spans  $r = 32$  cm to  $r = 45$  cm and is sufficiently covered by 21 chords. Thus, only one linear array was used to pass light to the detector, and one of the 22 fibers was placed in front of a neon calibration lamp in order to compensate for shot-to-shot variations in detector position on each shot. The spectrometer was calibrated to accommodate the configuration, and the dispersion of the full instrument was measured to be  $0.01326 \pm 5 \times 10^{-5}$  nm/pixel. With the slit properly affixed to the ferrule face the instrumental broadening is  $\approx 4.5$  pixels. Line integrated measurements clearly show a Doppler shift and broadening of the spectra as is evident in Fig. 6 which displays raw measurements along with the instrumental function for 4 channels measured on MRX shot 196543 in panel (a). Panel (b) shows the inverted profiles of  $E_0$ ,  $v_\phi$ , and  $T_i$  from top to bottom. Here, the units “Counts” for the  $E_0$  profile is a proxy for photons since the detector was not capable of being absolutely calibrated to obtain precise photon counts.

Plot (a) of Fig. 5 demonstrates the sensitivity of both  $T_i$  (green) and  $v_\phi$  (purple) inversions to the brightness level in the plasma. Plot (b) of Fig. 5 shows the simulated effect of radial flow magnitude (maroon), and uncertainty (cyan) in measured flow, on certainty in inverted  $T_i$  profiles. The effect on  $v_\phi$  profiles is not included since radial velocity does not affect the inversion for toroidal velocity.<sup>27</sup>

IV. RESULTS

More than three thousand shots in total were taken over the course of an extended experimental campaign in order to measure ion temperature and out-of-plane flow, as well as a variety of other plasma parameters that are needed to evaluate plasma stability, reproducibility, and possible mechanisms responsible for energy transfer during large guide field magnetic reconnection. In this section, a detailed description of experimental methodology is presented, followed by a description of the analysis techniques. Discussion of individual energization mechanisms is described in subsections therein.

For this experimental campaign, two high guide field conditions were explored using helium as a working gas. The firing conditions of each capacitor bank for  $B_{GF} \approx 1.4B_{rec}$  were TF = 9 kV, PF = 11 kV, Drive Coils = 5.7 kV, and  $B_{GF}$  was adjusted to produce a magnetic field component in the out-of-plane direction of  $\approx 90$  Gauss at the X-line. The firing conditions for  $B_{GF} \approx 2.1B_{rec}$  were TF = 11 kV, PF = 13 kV, Drive Coils = 6.3 kV, and  $B_{GF}$  was adjusted to produce a magnetic field component in the out of plane direction of  $\approx 115$  Gauss at the X-line. Both conditions utilized a counter-helicity configuration to reduce contributions to the guide field from sources other than the MRX GF coils in the center stack. The guide field current is ramped on the order of 10 ms making it effectively constant during the push and pull phases of reconnection which total less than 100  $\mu$ s. Drive coils, illustrated in Fig. 1, are employed to help drive reconnection which can be suppressed during high GF operation. This allows the experiment to remain in the regime, where  $E_y \geq 100$  V/m throughout. This regime is where outflow

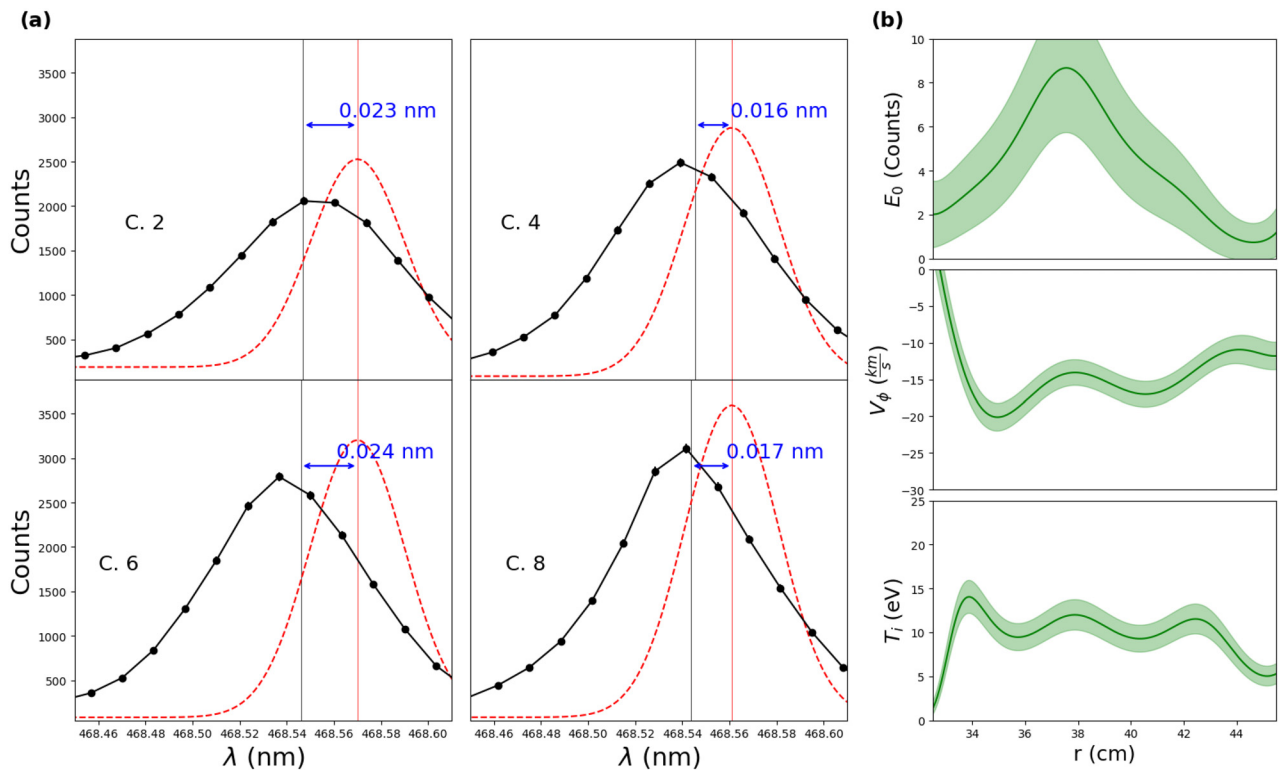


FIG. 6. (a) Raw measurements (black) and instrumental functions (red) for four measured channels for shot 196493. Shown with the associated inversion (b) on the right-hand side of the image. From the raw measurements compared to instrumental function, the shift in the negative direction and non-zero widths are apparent.

10 November 2023 16:29:01

is expected to approach Alfvén velocities. The coils have a secondary effect of helping to control the location of the X-line which has a tendency to drift in the  $z$  direction during high guide field operation in the absence of drive coils. A fill pressure of  $\approx 4.2$  mTorr of He gas is introduced for  $B_{GF} \approx 1.4B_{rec}$  and  $\approx 4.0$  mTorr is used for  $B_{GF} \approx 2.1B_{rec}$ . Lower pressures lead to X-line drift and diminished reproducibility, whereas higher fill pressures reduce the amount of available light and decrease the reconnection electric field below the 100 V/m target.

Reaching high guide field values used in this experimental campaign is a difficult undertaking in MRX due to X-line drift, low reconnection rates, and shot-to-shot variance. The two conditions utilized were chosen based on available light for ion Doppler diagnostics, reproducibility, and machine capability. Despite a focus on reproducibility, shot-to-shot variance precluded the use of 2-D profiles of *in situ* probe data obtained through Gaussian process regression (GPR),<sup>29</sup> except in the case of the B-dot probes. However, the data were sufficient to get measurements of local plasma parameters through alternative averaging methods, explained below. The values of these local parameters are shown in Table I. It is of note that the radial velocity near the X-line in the GF = 2.1 case is unexpectedly large. With both magnetic and density asymmetry across the X-line, it is estimated that the high total (magnetic and particle) pressure of the outboard region effectively “pushes” the stagnation point toward lower radial values on the inboard side of the plasma, creating a condition where there is non-negligible radial velocity at the X-line, due to a misalignment of the X-line and stagnation point in the plasma. This has been confirmed on MRX during anti-parallel reconnection.<sup>30</sup>

Throughout the experimental campaign, Langmuir and Mach probes were scanned as described in Sec. II. Langmuir probe, Mach probe, floating probe, and tomographic ion Doppler diagnostics are used for each shot. Data from electric probes, ion Doppler diagnostics, and magnetic probes are analyzed and utilized to help filter the dataset. A repeatable and consistent dataset suitable for averaging of local quantities is achieved by only examining shots with X-lines between  $37 \text{ cm} \leq r \leq 39 \text{ cm}$  and  $-1.5 \text{ cm} \leq z \leq 0.5 \text{ cm}$ , with reference Langmuir probe measurements that remain within 15% of average values, and reconnecting electric field  $E_y > 100 \text{ V/m}$  throughout the gate time of the ion Doppler diagnostic, which is  $10 \mu\text{s}$  from  $t = 335 \mu\text{s}$  to  $t = 345 \mu\text{s}$ . These shots are used to produce 2-D profiles of magnetics, ion temperature, and toroidal flow, as well as localized measurements from electrostatic probes of  $n_e$ ,  $T_e$ , and  $v_z$ . 2-D profiles are constructed with GPR on sufficient datasets of magnetics data and ion Doppler spectra. Localized measurements from *in situ* electrostatic probes are obtained using an averaging technique with a Gaussian kernel of  $r = 0.5 \text{ cm}$  around the point of interest to weight the impact of measurements within the zone of influence using techniques previously employed on MRX data.<sup>31,32</sup>

Figure 7 shows composite profiles for both  $T_i$  and  $v_\phi$  for both high-GF conditions. These profiles are created by averaging inversion results of many shots for each condition. Image accumulation is not used due to some variation in detector response shot-by-shot. All four profiles also show a line plot of a cut across  $z = 1.5 \text{ cm}$  below the 2-D profile. The left column of the figure shows results for  $v_\phi$ , and the right column shows results for  $T_i$ . The top row corresponds to  $B_{GF} \approx 2.1B_{rec}$ ,

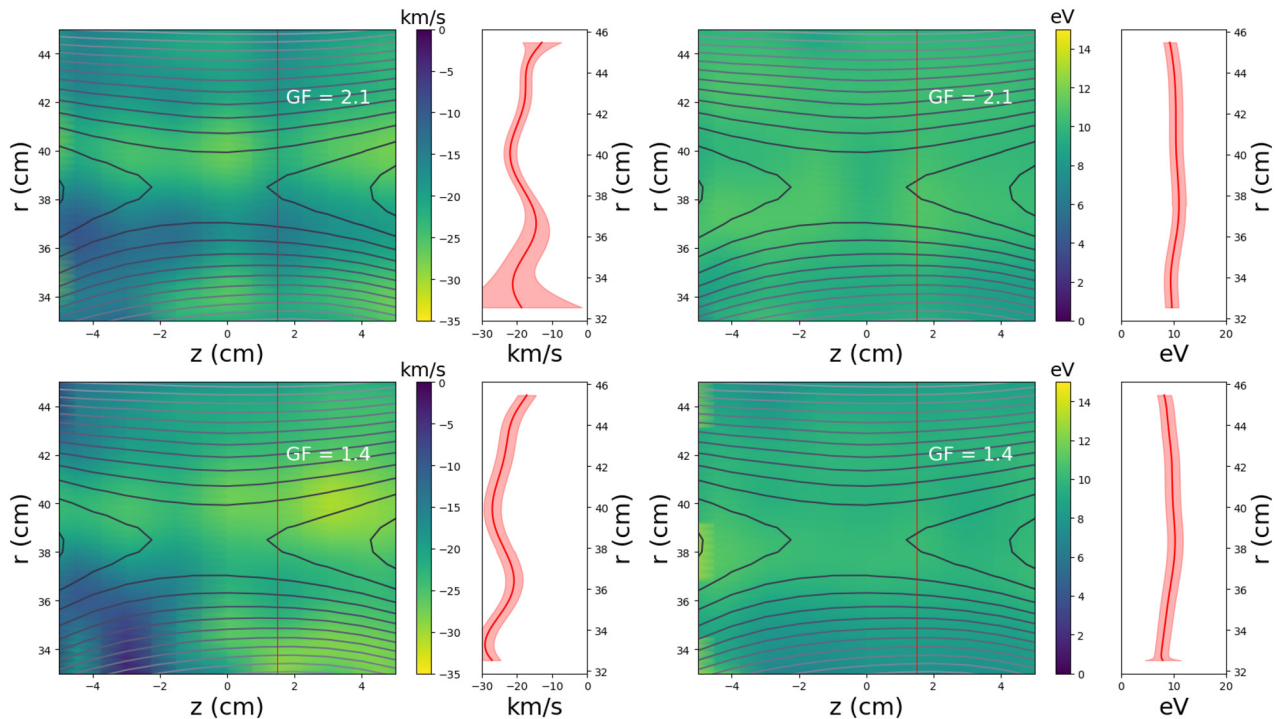


FIG. 7. Toroidal ion flow (left) and ion temperature (right) for GF = 2.1 (top) and GF = 1.4 (bottom) conditions measured by the tomographic ion Doppler spectroscopy diagnostic. Measurements are taken over tens gate times and are primarily flat in temperature. Note that the color schemes for temperature and velocity plots are inverted so that large magnitudes are always bright and lower magnitudes are darker.



and the bottom row corresponds to  $B_{GF} \approx 1.4B_{rec}$ . The profiles are built from averaging hundreds of profiles from similar shots, all using  $10 \mu\text{s}$  gate times, across a spatial grid.

The results show a relatively flat but sustained ion temperature of 7–11 eV, and a toroidal flow profile with large magnitude peaks ( $>20 \text{ km/s}$ ) near the reconnection layer. While there were non-negligible flows measured during anti-parallel or weak-guide field reconnection, this is the first time toroidal flows of this magnitude have been measured in MRX. For this experimental campaign, both GF conditions have ion skin depths larger than 2 cm and subsequently the true “downstream” region of the plasma is not measured by the tomographic diagnostic due to limitations of window size on MRX, compared with the other experiments in the downstream region where activity ion heating has been reported.<sup>9,10,16</sup>

Probe measurements are made in the downstream region, as far as  $z = 6 \text{ cm}$  for all probes, allowing for the estimation of various energization mechanisms, which are largely summarized in Table II, and described in Appendix. To estimate the effect of various mechanisms, a guiding center approximation is employed to probe possible particle energization during reconnection with sufficiently strong guide fields and with collisional effects ignored. While this method of estimation is useful in providing some context to the experiment and in guiding future experiment, it is limited by the weak adherence of the plasma to guiding center approximations, given that the ion gyroradius is on the order of the ion skin depth. Estimates presented in the following section are not meant to be interpreted as conclusions regarding the responsible source of ion energization.

To improve confidence in the capability of the diagnostic setup and inversion algorithm, data are taken from various diagnostic gate times to build a time series of ion temperature from  $t = 300 \mu\text{s}$  to  $t = 350 \mu\text{s}$ . Figure 8 shows the evolution of ion temperature at conditions similar to the GF = 1.4 condition used throughout the experiment and presented in Fig. 7. The shot conditions represented by each point vary slightly from the GF = 1.4 condition used for the bulk of this experiment including changes in the PF, TF, or SF firing voltages, and commiserate changes in the charging conditions of the Guide Field coils on MRX. Additionally, the points at  $t = 310 \mu\text{s}$  and  $t = 350 \mu\text{s}$  use a PF crowbar timing that is  $2 \mu\text{s}$  earlier than the timing used during the bulk of the experiment. For each shot, however, the guide field strength remains between 1.15 and 1.67 times the strength of the reconnecting field component. Each point represents 4–11 shots that have been accumulated to form a single image. The parabolic distortion of the images, created by the use of a linear slit on the optical input into the spectrometer, is removed, and the images from each of the 21 fibers are summed to create a single spectrum. That spectrum is fit, similar to the inversion technique, as a convolution of the instrumental function with the “true” Gaussian of emission. Unlike in the inversion process, for the accumulated images, a multi-Gaussian fit is used to better represent the data, which is less Gaussian due to the summation of data taken at various points within the plasma. Velocity is not shown in Fig. 8 due to a lack of calibration data for the detector position in the shots represented. This does not affect the temperature data as each point is comprised of an accumulation of consecutive images taken on a single day, giving confidence that the detector remains in the same position over each shot range. Figure 8 shows a meaningful increase in ion temperature starting for the gate time of  $t = 330 \mu\text{s}$  (point shown

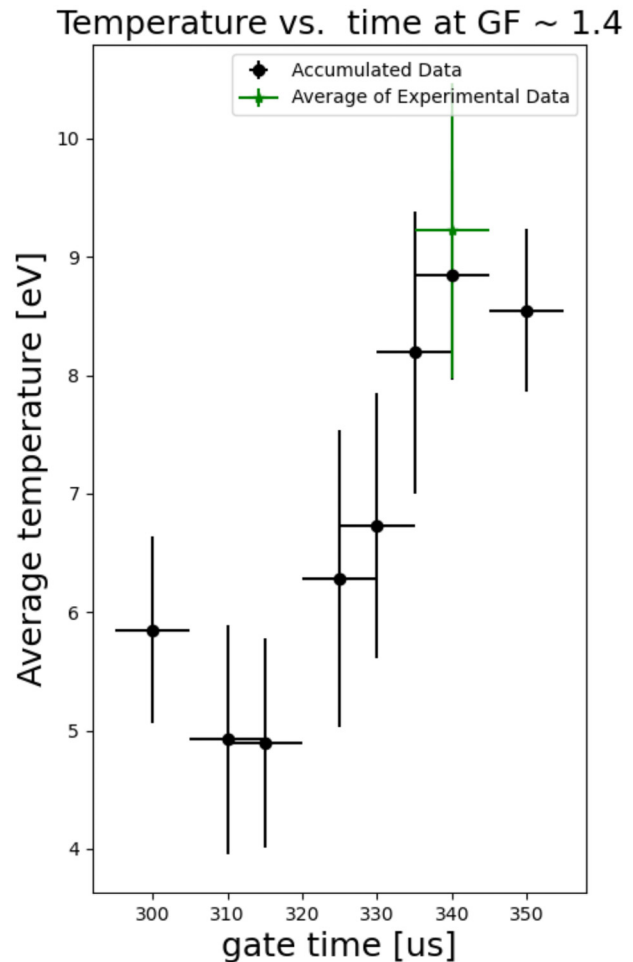


**FIG. 8.** Time series of ion temperature data taken during this experiment. Shots in black are calculated using accumulated images at each gate time to compensate for lower light levels at times proceeding  $t = 330 \mu\text{s}$ . The location of each point is centered on the middle of the gate time, and the errorbars extend  $5 \mu\text{s}$  in each direction to account for the  $10 \mu\text{s}$  gates used for each point. The average of data collected during the bulk of the experiment is shown in green. Velocity data are not shown in this figure due to the absence of shot-by-shot calibration data for all data sets.

at  $t = 335 \mu\text{s}$  representing the middle of the  $10 \mu\text{s}$  gate). The errorbars are large due to the combination of data from all radial measurement locations within the plasma and the limited number of shots available for each point; however, the data still suggest that the observed heating is related to reconnection dynamics. This observation suggests that more complete probe data, and a larger measurement window encompassing the downstream region of the plasma should help provide further clarity regarding the nature and source and ion heating at high guide field strengths.

## V. DISCUSSION

In this experimental campaign, a new diagnostic was constructed in order to measure line integrated emissivity, containing information about  $T_i$  and  $\nu_\phi$ , at a single  $z$  location for each shot taken on MRX.



By effectively scanning over different axial locations, the diagnostic enabled the construction of the first 2-D profiles of  $T_i$  and  $v_\phi$  during high GF reconnection on MRX. Profiles were constructed for two GF conditions,  $1.4 B_{\text{rec}}$  and  $2.1 B_{\text{rec}}$  where similar profiles were measured. These profiles showed relatively flat but sustained ion temperatures from 7 to 11 eV, and large, shallow peaks of  $v_\phi$  at magnitudes of  $\approx 20$  km/s. These results suggest significant levels of ion energization. No large out-of-plane velocity,  $v_\phi$ , was reported previously; however, comparison with  $E_y$  profiles suggests that the measured velocity is driven by the reconnection electric field within significant error bars. The minimal structure present in profiles of ion temperature and toroidal velocity shown in Fig. 7 is largely within errorbars and does not suggest any spatially resolved dynamics present in the measurement region. The lack of meaningful structure is likely a function of high shot-to-shot variation in critical fields, such as  $E_{\parallel}$ , as well as the location of the available measurement region, which was inside of the ion diffusion region for both guide field conditions. Further work in controlling the plasma at these high guide field conditions and expanding the measurement area is suggested. It is also of note that temporal data of ion temperature and toroidal velocity could not be measured during this experiment which leaves unresolved the question of whether ions are heated in the measurement region during the pull phase of reconnection or whether the temperature is simply sustained within this window. Drawing on the experimental results obtained during push reconnection at University of Tokyo,<sup>10</sup> it is expected that ions are energized during the push phase of reconnection, which precedes the pull phase. The outflowing ions of the push phase become the inflowing ions during the pull phase and, subsequently, is the population measured during this experiment. A more complete set of temporal measurements would also help to understand the nature of ion energization at high guide field strengths on MRX.

The operating conditions measured in this experiment are unique from previous work on MRX. This experiment measured higher magnitude toroidal flows and less structure in ion temperature than previous MRX work in the anti-parallel<sup>16</sup> and lower guide field regimes.<sup>9</sup> The results presented here extend beyond previous measurements at zero or lower guide fields on MRX and serve as a starting point for future exploration at increasingly high guide field values available on the Facility for Laboratory Reconnection Experiments (FLARE).<sup>24</sup> Other experiments have also measured ion temperature structure in the guide field regime<sup>10</sup> but in significantly different operating conditions. All other works have shown the majority of ion temperature increase to occur outside of the ion diffusion region.

Estimation of various energization mechanisms is made using ion Doppler measurements, as well as probe measurements from Langmuir probes, Mach probes, and a variety of magnetic probes used on MRX,<sup>33</sup> see Appendix. These estimates do not contain higher order terms which are expected to be non-negligible; however, they represent a starting point for understanding the nature of ion energization on MRX during high GF reconnection. Whereas previous analysis from Bose *et al.*<sup>9</sup> suggests that at lower GF conditions,  $\approx 0.7 B_{\text{rec}}$ ,  $E_{\perp}$  is the dominant mechanism of ion energization, this analysis at higher GF strengths suggests that  $E_{\parallel}$  plays an outsized role in energizing ions. There are two possible explanations for this result. One possibility is due to the fact that ion temperatures and velocities could not be measured outside of  $\pm 5$  cm away from the X-line axially. For this reason, the picture for the ion energization is incomplete, and in other regions,

$E_{\perp}$  may still play a significant role, that is not captured by the current measurement. Another possibility is that at stronger guide field strengths ions may remain, at least partially, magnetized in a larger region surrounding the X-line allowing for more direct acceleration from the electric field.

While the effects of various theoretical mechanisms such as the pickup mechanism<sup>17</sup> and stochastic heating<sup>18</sup> are estimated to be largely unimportant in these conditions, there is still significant work to be done to unlock the details behind ion energization in high GF reconnection. It is necessary to measure ion temperature and flow across a larger area of the reconnection layer. It is also desirable to take more detailed measurements to evaluate  $\mathbf{J} \cdot \mathbf{E}$ , with the breakdown between contributions from ions and electrons,  $\mathbf{J}_i \cdot \mathbf{E}$  and  $\mathbf{J}_e \cdot \mathbf{E}$ , respectively, and also for ions between parallel and perpendicular contributions,  $\mathbf{J}_{i,\parallel} \cdot \mathbf{E}_{\parallel}$  and  $\mathbf{J}_{i,\perp} \cdot \mathbf{E}_{\perp}$ , respectively. This work is expected to be continued on the upcoming FLARE.<sup>24</sup>

## ACKNOWLEDGMENTS

The authors would like to thank R. Bell, J. Jara-Almonte, W. Fox, and M. Yamada for their contributions to this research. The authors would also like to thank the journal referees for suggestions that improved the quality of this manuscript. This research is supported by Department of Energy Contract No. DE-AC02-09CH11466.

## AUTHOR DECLARATIONS

### Conflict of Interest

The authors have no conflicts to disclose.

## Author Contributions

**Aaron Goodman:** Conceptualization (equal); Data curation (lead); Formal analysis (lead); Investigation (lead); Methodology (equal); Software (lead); Visualization (lead); Writing – original draft (lead); Writing – review & editing (lead). **Hantao Ji:** Conceptualization (lead); Formal analysis (equal); Funding acquisition (lead); Methodology (equal); Project administration (lead); Supervision (lead); Validation (lead); Writing – review & editing (equal). **Sayak Bose:** Conceptualization (equal); Data curation (equal); Formal analysis (supporting); Investigation (supporting); Methodology (equal); Validation (equal); Writing – review & editing (equal). **Jongsoo Yoo:** Conceptualization (supporting); Data curation (supporting); Formal analysis (supporting); Investigation (supporting); Methodology (equal); Supervision (equal); Validation (equal); Writing – review & editing (equal). **Andrew Alt:** Investigation (supporting); Methodology (supporting); Writing – review & editing (equal).

## DATA AVAILABILITY

The data that support the findings of this study are available from the corresponding author upon reasonable request.

## APPENDIX: ENERGIZATION MECHANISMS

In the absence of complete 2-D plasma parameters, estimates of various energization mechanisms can be made by utilizing localized measurements in upstream and downstream regions. These measurements are incomplete and, thus, are left in the appendix of

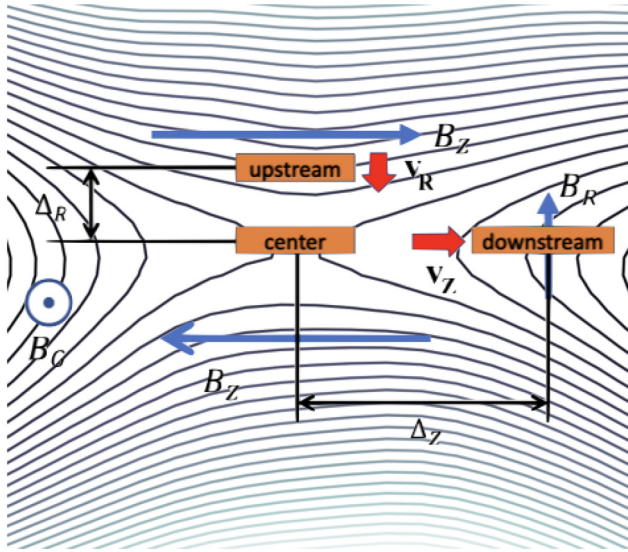


**FIG. 9.** Schematic drawing of MRX reconnection geometry, shown with a typical set of measured flux lines, and location of various measurement positions denoted “upstream” and “downstream.” Also shown are directions of magnetic field and flow components.  $\Delta_r$  and  $\Delta_z$  shown correspond to variables used throughout equations in Sec. IV. Region locations and sizes in the  $(z, R)$  coordinates are listed in Table I.

this document; however, they do provide important insight into future areas of research. The measurement locations and basic geometry are illustrated schematically in Fig. 9. For this analysis, upstream is defined as  $\Delta_r = 5$  cm above the X-line and the downstream region is defined at the furthest measurement made by all probes in the positive direction downstream from the X-line at  $z = 6$  cm, with symbols corresponding to the schematic in Fig. 9. The following estimates (other than the term on parallel electric field  $E_{\parallel}$ ) employ a guiding center approximation that is only weakly satisfied in the region of interest. The energization rate for ions during GF reconnection in a non-relativistic regime, ignoring collisional effects, is given by<sup>34</sup>

$$\frac{d\varepsilon}{dt} = qE_{\parallel}v_{\parallel} + \kappa \frac{dB}{dt} + q\mathbf{E} \cdot \mathbf{u}_e + \frac{1}{2}m \frac{d}{dt} |\mathbf{u}_E|^2, \quad (A1)$$

where  $\varepsilon$  is the total energy of the particle,  $\mathbf{u}_E = \mathbf{E} \times \mathbf{B}/B^2$ ,  $d/dt = \partial/\partial t + \mathbf{u}_E \cdot \nabla$ ,  $E_{\parallel}$  is the electric field parallel to the magnetic field,  $v_{\parallel}$  is the velocity of the guiding center approximation in the

parallel direction, and  $\kappa = mv_{\perp}^2/B$ . The terms on the right-hand side represent various mechanisms for energy gain that are represented in Table II. The following calculations are for the purpose of estimating four ion energization mechanisms during guide field reconnection on MRX. Error levels in Table II are between 15% and 35% depending on the quantity, but they do not affect the overall implied importance of each mechanism; however, combined with the aforementioned limitations on the method of estimation, the error of measured quantities further drives the need for follow-up experimentation. It is known that the guiding center approximation used for these estimates is only weakly satisfied due to the size of the ion gyroradius at experimental conditions. Since the ion gyroradius approaches the scale on which various quantities vary across the ion diffusion region, it is expected that the higher order terms are non-negligible, but they are ignored here due to the limited data available. Since we are interested in the relevance of each mechanism listed in Eq. (A1), the following is presented as our first attempt to estimate their relevance in our case.

### 1. Ion energization by $E_{\parallel}$

The contribution from  $E_{\parallel}$  is estimated inside the ion diffusion region (but outside of the electron diffusion region) where  $E_{\parallel}$  is given by  $\nabla_{\parallel} p_e/en$  during guide field reconnection, assuming uniform  $T_e$ ,<sup>31</sup>

$$E_{\parallel} \sim \frac{\nabla_{\parallel} p_e}{en} \sim \frac{[(n + \delta n) - (n - \delta n)]T_e}{en\Delta_z \sqrt{(B_G/B_z)^2 + 1}}, \quad (A2)$$

where  $p_e$  is the electron pressure and  $n$  is average electron number density between low and high density regions in the quadrupolar density structure during fast guide field reconnection.<sup>31</sup>  $\delta n$  is the difference in density in the regions of interest from the averaged density, and  $\Delta_z$  is the distance in the axial direction between low and high densities. Therefore,  $\Delta_z \sqrt{(B_G/B_z)^2 + 1}$  is the distance along the field line connecting low and high density regions in the upstream. The energy increase in ions due to the electric field between upstream and X-line regions is then estimated as  $\Delta T_i = eE_{\parallel}v_{\parallel}\Delta t$ , where  $v_{\parallel}$  is estimated as the out-of-plane velocity,  $v_{\phi}$  for ions and  $\Delta t$  is given as the time for ions to travel over the radial separation between the upstream and the X-line regions divided by the radial velocity. While  $v_{\phi}$  values are not shown in Table I, the 2-D profiles are shown in Fig. 7. For this experiment, the upstream region is defined 5 cm above the X-line region at

**TABLE I.** TABLE of region locations and plasma parameters used in calculations of various mechanisms discussed in Appendix.

Location or parameter	GF = 1.4			GF = 2.1		
	Upstream	Center	Downstream	Upstream	Center	Downstream
$(z, r)$ (cm)	$(-0.5 \pm 0.5, 43 \pm 0.5)$	$(-0.5 \pm 0.5, 38 \pm 0.5)$	$(6 \pm 0.5, 38 \pm 0.5)$	$(-1.0 \pm 0.5, 43.5 \pm 0.5)$	$(-1.0 \pm 0.5, 38.5 \pm 0.5)$	$(6 \pm 0.5, 38.5 \pm 0.5)$
$n$ ( $10^{13}/\text{cm}^3$ )	$2.1 \pm 0.8$	$5.5 \pm 1.2$	$2.3 \pm 0.7$	$4.9 \pm 1.6$	$1.6 \pm 0.8$	$2.3 \pm 0.5$
$T_e$ (eV)	$6.8 \pm 2.2$	$7.8 \pm 2.0$	$7.7 \pm 2.4$	$9.2 \pm 2.6$	$11.1 \pm 2.9$	$6.8 \pm 1.1$
$v_R$ (km/s)	$3.8 \pm 0.6$	$0.3 \pm 0.4$	$1.8 \pm 0.5$	$4.1 \pm 0.9$	$2.1 \pm 1.2$	$2.0 \pm 0.7$
$v_z$ (km/s)	$6.5 \pm 1.5$	$3.7 \pm 0.6$	$4.1 \pm 0.9$	$6.0 \pm 1.4$	$1.4 \pm 0.6$	$7.5 \pm 1.7$

**TABLE II.** Estimate of energy increase,  $\Delta\epsilon$ , by each ion energization mechanism for both high guide field conditions, except in the last row where typical values of ion-ion collision time are listed.

Mechanism	Upstream $\rightarrow$ center		Center $\rightarrow$ downstream	
	GF = 1.4 (eV)	Gf = 2.1 (eV)	GF = 1.4 (eV)	GF = 2.1 (eV)
$E_{\parallel}$	3.51	3.92	4.37	5.73
Betatron heating	0.31	0.76	0.60	0.55
Curvature drift	0.08	0.09	0.18	0.08
Polarization drift	0.72	0.86	0.85	2.79

$\Delta_r = 5 \pm 0.5$  cm and the downstream region is defined at  $z = 6$  cm, the furthest downstream measurement taken by the Langmuir probe. To examine the energy increase from the x-line to the downstream region, all “z” subscripts in Eq. (A2) are replaced by “r” subscripts,  $\Delta_r$  is replaced by  $\Delta_z$ , and  $\Delta_r$  is replaced by  $\Delta_z$ . The calculations shown in Table II suggest that of the estimated mechanisms for ion energization; the parallel electric field may serve as an important source of energization. This suggestive evidence stands in contrast to the results collected at lower guide field strengths in MRX, including the conclusions from Bose *et al.*<sup>9</sup> which suggests that  $E_{\perp}$  is mainly responsible for ions to gain energy at a weak guide condition of  $B_{GF} \approx 0.7B_{rec}$ . Due to the observed sustained heating and high velocity throughout the measurement region, it is possible that only a fraction of the ion population crosses through the X-line and moves downstream, experiencing the estimated effects of mechanisms in Table II. In this case, it is theorized that most ion move across the separatrix. This explanation could not be probed in the experiment but may be better evaluated in future works.

## 2. Energization by Betatron acceleration, curvature drift, and polarization drift

Betatron acceleration changes perpendicular energy due to  $\nabla B$  drift and is defined by

$$\Delta T_i = \mu_i \frac{dB}{dt} \Delta t = \frac{4eT_i}{3B} (\mathbf{u}_E \cdot \nabla) B \Delta t. \quad (\text{A3})$$

This mechanism is estimated to be relatively unimportant in the energization of ions in our case. Curvature drift can drive parallel heating through Fermi reflection and is equally unimportant. It can be described by

$$\Delta T_i = qE \cdot \mathbf{u}_c \Delta t = \frac{2eT_i}{3B} \mathbf{E} \cdot (\mathbf{b} \times \boldsymbol{\kappa}) \Delta t, \quad (\text{A4})$$

where  $\boldsymbol{\kappa} = \mathbf{b} \cdot \nabla \mathbf{b} \sim 1/r_c$ , where  $\mathbf{b}$  is magnetic unit vector and  $r_c$  is the curvature radius which can be on the order of system size in the upstream region. Polarization drift is calculated as

$$\Delta T_i = \frac{1}{2} m_i (\mathbf{u}_E \cdot \nabla) |\mathbf{u}_E|^2 \Delta t \quad (\text{A5})$$

and is small compared to  $E_{\parallel}$  everywhere except in the center to downstream region for the GF = 2.1 case where the polarization drift may contribute meaningfully to ion heating from the estimation in Table II. This is largely caused by the fast outflow in this condition, nearly double outflow of the GF = 1.4 condition, as can be seen in Table I.

## 3. Collisional heating, stochastic heating, and energization by ion pickup process

Collision times for ions are calculated as  $1/\nu_i$ , where collision frequency,  $\nu_i$ , is given by<sup>35</sup>

$$\nu_i = 4.8 \times 10^{-8} Z^4 \mu^{-\frac{1}{2}} n_i \ln(\Lambda) T_i^{\frac{3}{2}} \text{sec}^{-1}. \quad (\text{A6})$$

Since the gate time of the diagnostic is 10  $\mu\text{s}$ , there is incomplete evidence that collisional heating also contributes to the thermalization of ions during the measurement period. Due to the nominal densities for this experiment which are  $n_i \approx 4 \times 10^{13} \text{cm}^{-3}$  for GF 1.4 and  $n_i \approx 2 \times 10^{13} \text{cm}^{-3}$  for GF 2.1 and results from previous experiments,<sup>9,16</sup> it is likely that collisions play some role in the thermalization of ions; however, the data collected here is not capable of advancing that argument.

In addition to the mechanisms described above, the criteria for ion pickup heating<sup>17</sup> and stochastic heating<sup>18,36</sup> mechanisms are examined for this experiment. The mechanism of pickup-particle heating was first described by Möbius *et al.*<sup>37</sup> and extended by Drake *et al.*<sup>17</sup> who formulated a concise criteria for evaluating the relevance of pickup-like behavior.

$$\frac{m_i}{Z_i m_p} > \frac{1}{R_r \pi \sqrt{2}} \sqrt{\beta_{up}}. \quad (\text{A7})$$

In Eq. (A7),  $R_r$  is the normalized reconnection rate and  $\beta_{up}$  is the ratio of plasma to magnetic pressure in the upstream region. For this experiment, the relationship does not hold as true for either GF condition in the relevant area upstream of the reconnection x-line region.

Stochastic heating of ions can occur when strong perpendicular electric field can chaotize particle orbits and effectively heat particles due to phase-space broadening. Yoon and Bellan<sup>18</sup> extended this concept to include another metric to easily assess the viability of stochastic heating in a given regime as

$$\frac{m_i}{q_i |B|^2} |\nabla_{\perp} \cdot \mathbf{E}_{\perp}| > 1. \quad (\text{A8})$$

Calculation of this condition shows no regions of applicability at very high GF (GF = 2.1) and only limited application near the x-line for GF = 1.4. This suggests that that stochastic heating and the effects of  $E_{\perp}$  may be unimportant at higher GF conditions. These estimates are consistent with measurements made by the new ion Doppler diagnostic which shows large toroidal flows sustained at various high GF conditions measured in this experiment. These flows, which are often in excess of 20 km/s in magnitude, must be generated from a directed and readily available force in the plasma. For this experiment,  $E_{\parallel}$  is a likely source.

## REFERENCES

- <sup>1</sup>D. Biskamp, *Magnetic Reconnection in Plasmas* (Cambridge University Press, 2000).
- <sup>2</sup>J. Dahlin, J. Drake, and M. Swisdak, *Phys. Plasmas* **21**, 092304 (2014).



- <sup>3</sup>H. Tanaka, H. Tanaba, Q. Cao, and Y. Ono, *Plasma Fusion Res.* **16**, 2402068 (2021).
- <sup>4</sup>R. Ergun, K. Goodrich, F. Wilder, J. Holmes, J. Stawarz, S. Eriksson, A. Sturmer, D. Malaspina, M. Usanova, R. Torbert *et al.*, *Phys. Rev. Lett.* **116**, 235102 (2016).
- <sup>5</sup>F. Wilder, R. Ergun, S. Eriksson, T. Phan, J. Burch, N. Ahmadi, K. Goodrich, D. Newman, K. Trattner, R. Toerber *et al.*, *Phys. Rev. Lett.* **118**, 265101 (2017).
- <sup>6</sup>Z. Li and M. Zhang, *Astrophys. J.* **888**, 5 (2019).
- <sup>7</sup>T. Phan, S. Bale, J. Eastwood, B. Lavraud, J. Drake, M. Oiseroset, M. Shay, M. Pulpala, M. Stevens, R. MacDowall *et al.*, *Astrophys. J. Suppl. Ser.* **246**, 34 (2017).
- <sup>8</sup>B. Chen, C. Shen, D. Gary, K. Reeves, G. Fleishman, S. Yu, F. Guo, S. Krucker, J. Lin, G. Nita *et al.*, *Nat. Astron.* **4**, 1140 (2020).
- <sup>9</sup>S. Bose, W. Fox, H. Ji, J. Yoo, A. Goodman, A. Alt, J. Jara-Almonte, and M. Yamada, "Conversion of magnetic energy to plasma kinetic energy during guide field magnetic reconnection the laboratory," (in press) (2022).
- <sup>10</sup>H. Tanabe, A. Kuwahata, H. Oka, M. Annoura, H. Koike, K. Nishida, S. You, Y. Narushima, A. Balandin, M. Inomoto, and Y. Ono, *Nucl. Fusion* **53**, 093027 (2013).
- <sup>11</sup>R. Granetz and P. Smeulders, *Nucl. Fusion* **28**, 457 (1988).
- <sup>12</sup>M. Yamada, R. Kulsrud, and H. Ji, *Rev. Mod. Phys.* **82**, 603 (2010).
- <sup>13</sup>A. Goodman, J. Yoo, J. Jara-Almonte, and H. Ji, *Rev. Sci. Instrum.* **92**, 063508 (2021).
- <sup>14</sup>M. Yamada, H. Ji, S. Hsu, T. Carter, R. Kulsrud, N. Bretz, F. Jobses, Y. Ono, and F. Perkins, *Phys. Plasmas* **4**, 1936–1944 (1997).
- <sup>15</sup>G. Fiksel, D. Hartog, and P. Fontana, *Rev. Sci. Instrum.* **69**, 2024 (1998).
- <sup>16</sup>M. Yamada, J. Yoo, J. Jara-Almonte, H. Ji, R. Kulsrud, and C. Myers, *Nat. Commun.* **5**, 4774 (2014).
- <sup>17</sup>J. Drake, M. Swisdak, T. Phan, P. Cassak, M. Shay, S. Lepri, R. Lin, E. Quataert, and T. Zurbuchen, *J. Geophys. Res.* **114**, A05111, <https://doi.org/10.1029/2008JA013701> (2009).
- <sup>18</sup>Y. Yoon and P. Bellan, *Astrophys. J. Lett.* **887**, L29 (2019).
- <sup>19</sup>W. Fox, F. Wilder, S. Eriksson, J. Jara-Almonte, F. Pucci, J. Yoo, H. Ji, M. Yamada, R. Ergun, M. Oiseroset *et al.*, *Geophys. Res. Lett.* **45**, 12677–12684, <https://doi.org/10.1029/2018GL079883> (2018).
- <sup>20</sup>J. Egedal, W. Daughton, J. F. Drake, N. Katz, and A. Lê, "Formation of a localized acceleration potential during magnetic reconnection with a guide field," *Phys. Plasmas* **16**, 050701 (2009).
- <sup>21</sup>K. Genestreti, J. Burch, P. Casak, R. Torbert, R. Ergun, A. Varsani, T. Phan, B. Giles, C. Russell, S. Wang *et al.*, *J. Geophys. Res. Space Phys.* **122**, 11342–11353, <https://doi.org/10.1002/2017JA024247> (2017).
- <sup>22</sup>J. Jara-Almonte, H. Ji, M. Yamada, J. Yoo, and W. Fox, "Laboratory observation of resistive electron tearing in a two-fluid reconnecting current sheet," *Phys. Rev. Lett.* **117**, 095001 (2016).
- <sup>23</sup>J. Yoo, "Experimental studies of particle acceleration and heating during magnetic reconnection," Ph.D. dissertation (Princeton University, Program in Plasma Physics, 2013).
- <sup>24</sup>H. Ji, R. Cutler, G. Gettelfinger, K. Gilton, A. Goodman, F. Hoffmann, J. Jara-Almonte, T. Kozub, J. Kukon, G. Rossi, P. Sloboda, J. Yoo, and FLARE Team, "The FLARE device and its first plasma operation," in *APS Division of Plasma Physics Meeting Abstracts* (APS Meeting Abstracts, 2018), Vol. 2018, p. CP11.020.
- <sup>25</sup>S. Barden, *Pub. Astron. Soc. Pacific* **112**, 809–820 (2000).
- <sup>26</sup>J. Weaver, G. Holland, U. Feldman, J. Seely, C. Brown, V. Serlin, A. Deniz, and M. Klapisch, *Rev. Sci. Instr.* **72**, 108 (2001).
- <sup>27</sup>R. E. Bell, *Plasma Phys. Control Fusion* **63**, 045023 (2021).
- <sup>28</sup>R. H. Byrd, R. B. Schnabel, and G. A. Shultz, "Approximate solution of the trust region problem by minimization over two-dimensional subspaces," *Math. Program.* **40**, 247–263 (1988).
- <sup>29</sup>C. Rasmussen, *Gaussian Processes for Machine Learning* (MIT Press, 2005).
- <sup>30</sup>J. Yoo, M. Yamada, H. Ji, J. Jara-Almonte, C. E. Myers, and L.-J. Chen, "Laboratory study of magnetic reconnection with a density asymmetry across the current sheet," *Phys. Rev. Lett.* **113**, 095002 (2014).
- <sup>31</sup>W. Fox, F. Sciortino, A. Stechow, V. J. Jara-Almonte, J. Yoo, H. Ji, and M. Yamada, "Experimental verification of the role of electron pressure in fast magnetic reconnection with a guide field," *Phys. Rev. Lett.* **118**, 125002 (2017).
- <sup>32</sup>W. Fox, J. Jara-Almonte, J. Yoo, H. Ji, M. Yamada, and A. V. Stechow, "Electromagnetic fluctuations during guide field reconnection in a laboratory plasma," *Phys. Plasmas* **25**, 052120 (2018).
- <sup>33</sup>J. Yoo, M. Yamada, H. Ji, J. Jara-Almonte, and C. Myers, *Phys. Plasmas* **21**, 055706 (2014).
- <sup>34</sup>H. Ji, W. Daughton, J. Jara-Almonte, A. Le, A. Stainer, and J. Yoo, *Nat. Rev. Phys.* **4**, 263–282 (2022).
- <sup>35</sup>S. Braginskii and M. Leontovich, *Reviews of plasma physics* (1965).
- <sup>36</sup>A. Stark, W. Fox, J. Egedal, O. Grulke, and T. Klinger, "Laser-induced fluorescence measurement of the ion-energy-distribution function in a collisionless reconnection experiment," *Phys. Rev. Lett.* **95**, 235005 (2005).
- <sup>37</sup>E. Mobius, D. Hovestadt, B. Klecker, M. Scholer, G. Gloeckler, and F. Ipavich, *Nature* **318**, 426–429 (1985).